Journal of Colloid and Interface Science 694 (2025) 137630

Contents lists available at ScienceDirect

Journal of Colloid And Interface Science

journal homepage: www.elsevier.com/locate/jcis

Regular Article

In-situ transformation of a conjugated nickel-organic framework into active nickel oxyhydroxide for electrocatalytic 5-hydroxymethylfurfural oxidation

Abdul Khayum Mohammed [a,1], J. Niklas Hausmann [b,1], Safa Gaber [a,1], Pilar Pena Sánchez [c], Felipe Gándara [c], Konstantin Laun [d], Ingo Zebger [d], Prashanth W. Menezes [b,e,*], Dinesh Shetty [a,f,**]

[a] Department of Chemistry, Khalifa University of Science & Technology, PO Box: 127788, Abu Dhabi, United Arab Emirates
[b] Department of Materials Chemistry for Catalysis, Helmholtz-Zentrum Berlin für Materialien und Energie, Albert-Einstein-Str. 15, 12489 Berlin, Germany
[c] Instituto de Ciencia de Materiales de Madrid-CSIC, C/Sor Juana Inés de la Cruz 3, 28049 Madrid, Spain
[d] Department of Chemistry: Physical Chemistry/Biophysical Chemistry, Technische Universität Berlin 10623 Berlin, Germany
[e] Department of Chemistry, Metalorganics and Inorganic Materials, Technische Universität Berlin, Straße des 17 Juni 135, Sekr. C2, 10623 Berlin, Germany
[f] Center for Catalysis and Separations (CeCaS), Khalifa University of Science & Technology, PO Box: 127788, Abu Dhabi, United Arab Emirates

HIGHLIGHTS

- Scalable solid-state synthesis of Ni-based conjugated metal–organic framework.
- The conjugated MOF showed 40 μS m^{-1} (25 kΩ m^{-1}) at room temperature.
- A highly selective electrocatalytic conversion of HMF into FDCA (96 ± 4 %) is achieved.
- MOF is a source of active catalyst (NiOOH) and an electron conductive platform.
- In-situ Raman and XAS revealed the synergic effect of MOF and NiOOH in catalysis.

GRAPHICAL ABSTRACT

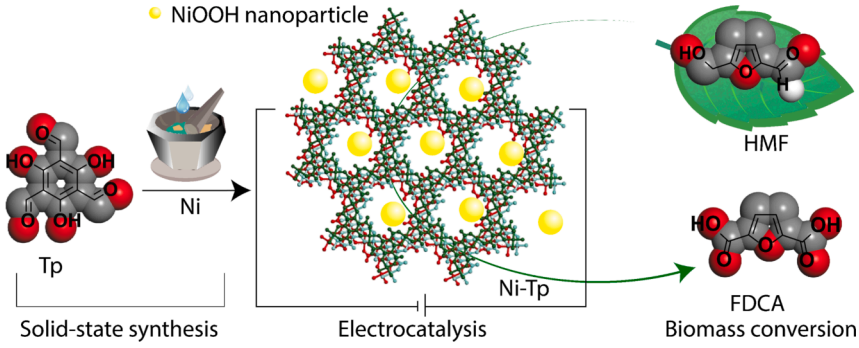

ARTICLE INFO

Keywords:
Metal organic frameworks
Conjugated MOFs
Electrocatalysis
Green synthesis
HMF conversion
In-situ spectroscopy
Organic oxidation reaction (OOR)

ABSTRACT

Utilizing electrical energy for the targeted conversion of biomass into valuable molecules is a crucial building block for a future circular economy. Herein, a Nickel (Ni)-based conjugated metal–organic framework (MOF) having salicylaldehydate linkages (1, 3, 5-triformylphloroglucinol: Tp) was synthesized via a solid-state process. The resulting 2D framework (Ni-Tp) demonstrates a highly selective electrocatalytic conversion of 5-hydroxymethylfural (HMF) to 2, 5-furandicarboxylic acid (FDCA) with excellent faradaic efficiency (96 ± 4 %). In-situ Raman and X-ray absorption spectroscopy (XAS) reveal that Ni-Tp acts as a precatalyst for uniformly dispersed nickel (oxy)hydroxide (NiOOH) in the electrocatalytic organic oxidation reaction (OOR) process. The combination of efficient electron transport of the Ni-Tp and the uniform dispersion of newly formed nickel (oxy)

* Corresponding author at: Department of Materials Chemistry for Catalysis, Helmholtz-Zentrum Berlin für Materialien und Energie, Albert-Einstein-Str. 15, 12489 Berlin, Germany.
** Corresponding author at: Department of Chemistry, Khalifa University of Science & Technology, PO Box: 127788, Abu Dhabi, United Arab Emirates.
E-mail addresses: prashanth.menezes@mailbox.tu-berlin.de (P.W. Menezes), dinesh.shetty@ku.ac.ae (D. Shetty).
[1] These authors contributed equally.

https://doi.org/10.1016/j.jcis.2025.137630
Received 19 November 2024; Received in revised form 8 April 2025; Accepted 15 April 2025
Available online 21 April 2025

hydroxide with excellent electrolyte availability leads to redox (and potentially catalytic) activity of all in situ formed nickel sites. Thus, the Ni-Tp is an ideal precatalyst in terms of nickel (oxy)hydroxide active site exposure. This work demonstrates a cost-effective method for synthesizing efficient MOF-based electrocatalysts for a relevant catalytic reaction.

1. Introduction

Metal-organic frameworks (MOFs) are two- or three-dimensional (2D/3D) inorganic–organic hybrid porous materials with well-defined structures [1]. The wide variety of metal nodes and organic linkers has enabled the preparation of diverse functional porous structures. Among these, π-d conjugated two-dimensional MOFs (2D-*c*-MOFs) are known for their optoelectronic properties due to the coordination of vacant d orbitals of metal ions with π orbitals of organic building blocks [2–5]. Specifically, 2D-c-MOFs are being investigated for their electrocatalytic potential due to their high surface-to-volume ratio, inherent electronic mobility, and uniform distribution of metal centers [6]. Recently, MOF-based catalysts/precatalysts were explored for the transformation of biomass-derived 5-hydroxymethylfural (HMF) into value-added 2, 5-furandicarboxylic acid (FDCA) [7,8]. HMF can be derived from abundant and cheap lignocellulosic biomass, and FDCA is a precursor for green polymer production [7,8]. The targeted conversion of biomass into such valuable molecules presents a promising strategy for advancing the circular economy. Significant research has been done on the electrical energy-induced transformation of such molecules [9]. Notably, c-MOFs were predominantly synthesized using solvothermal synthetic strategies [10–13]. Meanwhile, applications like biomass conversion into commercially valuable chemicals require highly efficient catalysts/precatalysts on a large scale. In this regard, producing electrocatalysts more cost-effectively, preferably through solvent-free methods, is advisable. Notably, solid-state synthesis, often considered an efficient, scalable, and economical method, presents itself as a viable alternative.

Considering all these aspects, we have synthesized a nickel (Ni)-based 2D-c-MOF (Ni-Tp) through a solid-state mechanomixing process. Herein, the Ni atoms are connected via salicylaldehydate linkages of an organic linker; 1, 3, 5-triformylphloroglucinol (Tp), i.e., ortho aldehyde (−H–C═O) and hydroxyl (–OH) functional groups, forming a 2D framework [14]. In this work, the dynamic properties of Ni centers in the framework were explored for the selective electrocatalytic conversion of HMF to FDCA. In the electrocatalytic process, Ni-Tp plays the following crucial roles: 1) It serves as a source of active electrocatalytic sites, namely nickel (oxy)hydroxide, and 2) acts as the electron transport platform. The π-d conjugation in Ni-Tp enables local electron transport throughout the system (conductivity of ~40 μS m^{-1} (25 kΩ m^{-1}) at room temperature), contributing to enhanced catalytic activity. As a result of the synergic effect of Ni-Tp/NiOOH, the electrocatalytic investigation showed the conversion of HMF into FDCA with 96 ± 4 % selectivity and faradaic efficiency. Furthermore, the detailed ex-situ and in-situ characterizations evidenced the partial reconstruction of Ni-Tp into nickel (oxy)hydroxide nanoparticles. Significantly, these newly formed Ni sites exhibit a potential-dependent high redox activity transitioning between nickel hydroxide and nickel (oxy)hydroxide. Combining scalable production methods and the synergistic effect of Ni-Tp and NiOOH underscores its practical applicability in large biomass conversion to valuable chemicals.

2. Experimental

2.1. Synthesis of Ni-Tp

The Ni-Tp was synthesized through mechanochemical reactions using a mortar and pestle. The Tp linker (0.15 mmol) was directly added into the 1.5 equivalent of $Ni(CH_3CO_2)_2{\cdot}4H_2O$ (0.225 mmol) and mechano-mixed thoroughly into a solid paste form (Fig. 1a and Fig. S1). A drop of deionized (DI) water (~50 μL) was added to the solid mixture for uniform mixing and subsequently heated at 90° C in a closed container for 5 h. The resulting solid powder was washed with *N,N*-dimethylacetamide (DMA), tetrahydrofuran (THF), water, and acetone to obtain Ni-Tp. [Synthetic procedures for all compounds are given in SI.].

2.2. Electrochemical measurements

Electrochemical experimental setups: A standard three-electrode (working, counter, and reference) electrochemical cell with 10 ml electrolyte (1.0 M aqueous KOH (pH 13.89)[1] with the respective HMF concentration) and a potentiostat (SP–200, BioLogic Science Instruments) controlled by the EC-Lab v10.20 software package was utilized for the measurements. Nickel foam and (NF) and fluorine-doped tin oxide glass plates (FTO) with thin films of the respective compounds were used as the working, Pt wire (0.5 mm diameter × 230 mm length, A-002234, BioLogic) as the counter electrode, and Hg/HgO (RE-61AP, BAS Inc.) as the reference electrode. The Hg/HgO potentials were referenced to the reversible hydrogen electrode (RHE) through calibration with a self-made RHE. This method utilizes two platinum foils as the working and counter electrodes and the Hg/HgO electrode as the reference electrode. With these electrodes, CVs are performed in the electrolyte (organic substrate + 1 M aqueous KOH), which was saturated with hydrogen gas through bubbling for 1 h before measurement. The point at which the current density reaches zero (approximately −934 mV) was taken as the RHE potential.

Electrophoretic sample deposition (EPD): The materials were electrophoretically deposited using a well-established, binder-free procedure on nickel foam (NF) and fluorine-doped tin oxide glass plates (FTO). In a two-electrode setup with FTO or nickel foam (2 × 1 cm^2) serving as the counter and reference electrodes, and a mixture of iodine, catalyst powder, and acetone as the electrolyte, a potential difference is applied, resulting in the deposition of a beige film on the cathode. In this process, keto-enol tautomerization of acetone leads to a reaction with iodine, producing protons. These protons are adsorbed on the surface of the suspended particles, leading to a positive surface charge. This charge enables the particles to migrate along the applied electric field toward the cathode where they deposit. In the standard procedure, 25 mg of Ni-Tp was suspended in 8 ml acetone and sonicated at room temperature for 3 h. Then, 3 mg of iodine was added, and the suspension was sonicated for three additional minutes. Immediately after the sonication, EPD was performed at 10 V for 60 s while stirring to obtain uniform films. The sample loading was determined by weighing the NF and FTO before and after the deposition process (error approximately 0.1 mg/cm^2) and was found to be 0.6 and 0.3 mg/cm^2, respectively.

iR compensation: The uncompensated resistance (R_u) was determined through impedance spectroscopy with 100 MHz, an amplitude of 10 mV, and at a potential of 1.175 V_{RHE} before each measurement. It was found to be usually in the range of 0.8 Ω for NF and 10 Ω for FTO. The potential was corrected by 90 % of R_u.

Linear scan voltammetry: LSVs were recorded at 10 mV s^{-1} without stirring, if not stated otherwise, and *iR* compensation.

Chronoamperometry and chronopotentiometry: The CA and CP measurements were performed with stirring and an applied *iR* compensation of 90 %. Additionally, the electrolyte was temperature-controlled at 25 °C.

HMF bulk electrolysis: Bulk electrolysis was performed under constant

potential (1.47 V_{RHE}) with stirring at 500 rpm (15 ml beaker, 1 cm stirring bar, 1.5 cm diameter) with 10 ml electrolyte. The HMF was added to the KOH just before the potential was applied to minimize the formation of side products through reactions that are not potential-driven.

Characterization of HMF oxidation products: The oxidation reaction mixture was characterized by ^{1}H nuclear magnetic resonance spectroscopy (^{1}H NMR) spectroscopy in a 400 MHz JEOL NMR and Bruker AV400 instrument. The internal standard (maleic acid, 52 mg) was diluted in 1 ml D_2O and then added to this solution (10 µl per NMR tube) with a transfer pipette. The molar concentration of maleic acid in the NMR tube was identical to the initial concentration of HMF (typically 30 mM). The ^{1}H NMR sample was prepared by taking a 150 µL aliquot of the reaction mixture solution and 350 µL D_2O solvent. Processing and plotting of the spectra were performed using MestReNova software. A sharp peak at 4.7 ppm appeared for the H_2O from the aqueous reaction mixture and was used as a reference for the chemical shifts of the other proton signals. The chemical shift values of the protons of the organic products were assigned accordingly. The HMF oxidation product (FDCA) was quantified (chemical conversion) by calculating the relative intensity of the proton signals in comparison to the internal standard. Chemical conversion and Faradaic efficiency (FE) were calculated using the following equations:

$$Chemical\ conversion(\%) = \left[n_{product}/n_{reactant\ initial\ conc.}\right]x100 \quad (3)$$

$$FE(\%) = \left(n_{product}\cdot n_e\cdot F/Q\right)x100 \quad (4)$$

where *FE* is the Faradaic efficiency, *F* is the Faraday constant (96,485 C mol^{-1}), *n* is the mol of reactant quantified from ^{1}H NMR, n_e is the number of electrons needed for the oxidation process (6 for HMF to FDCA), and *Q* is the charge (coulombs) passed in the electrochemical cell. The error (±4%) provided for the Faradaic efficiency determination of this reaction is based on the standard deviation of three independent bulk oxidations with three different electrodes using powder from the same Ni-Tp synthesis batch.

3. Results and discussion

3.1. Characterizations of material

The structural periodicity of Ni-Tp was evident from the powder X-ray diffraction (PXRD) profile (Fig. 1c; Figs. S2–S4). The broadness of the peaks indicates the semi-crystallinity of the material. The diffraction peaks of Ni-Tp originated at two theta ~7.0°, ~14.2°, ~20.3°, ~25.2°, and ~28.5°. To decipher the possible structure of Ni-Tp, theoretical crystal models were simulated using Material Studio software (Fig. 1b; d–f and Table S1). The theoretical model was optimized with Ni^{2+} atoms at the metal position in the $P3_1$ space group ($a = b = 14.55$ Å and $c = 9.37$ Å). In this model, the Ni^{2+} atoms were coordinated with two salicylaldehyde functional pockets from separate Tp molecules [14]. Notably, the 2D layers of Ni-Tp are not fully eclipsed in nature, instead, a slight displacement of Ni atoms and aldehyde oxygen of adjacent layers was noted in the optimized structure (hcb layers with ABC stacking).

The chemical bonding features of Ni-Tp were inspected using Fourier-transform infrared (FT-IR) spectroscopy (Fig. 2a and Fig. S5). The peak shifting of aldehyde C═O (1619 cm^{-1}) to a lower frequency of 1550 cm^{-1} could indicate the coordinative interaction of Ni^{II} with the C═O group, which may weaken the double bond between carbon and oxygen and decrease the vibrational frequency between them. Furthermore, X-ray photoelectron spectroscopy (XPS) revealed the chemical states of elements in Ni-Tp (Fig. 2b and Fig. S6). The XPS profile of Ni-Tp showed two significant peaks corresponding to Ni $2p_{3/2}$ (856.42 eV) and

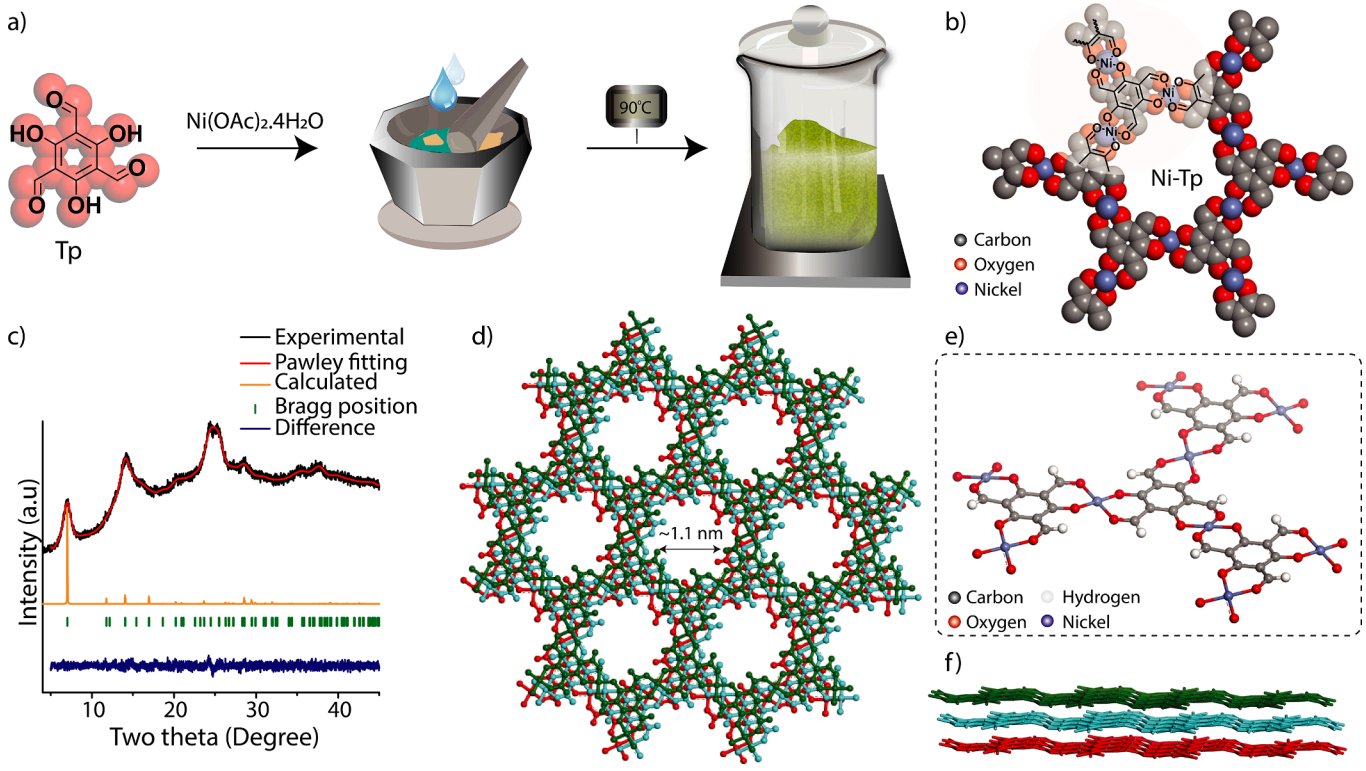

Fig. 1. (a) graphical representation of the synthesis of Ni-Tp from the organic building block (Tp) and metal ions (Ni^{2+}). (b) The hexagonal network of Ni-Tp with the chemical structure. (c) Experimental (black) and calculated (orange) PXRD profiles of Ni-Tp, along with the Bragg positions (green), the difference between both patterns (blue), and the Pawley refinement (red). (d) The square planar model of Ni-Tp (Pore size: ~1.1 nm and an interlayer distance of ~0.3 nm. (e) The 2D square planar bonding of Tp with Ni. (f) The three consecutive layers of Ni-Tp with an interplanar distance of ~ 0.3 nm. (For interpretation of the references to color in this figure legend, the reader is referred to the web version of this article.)

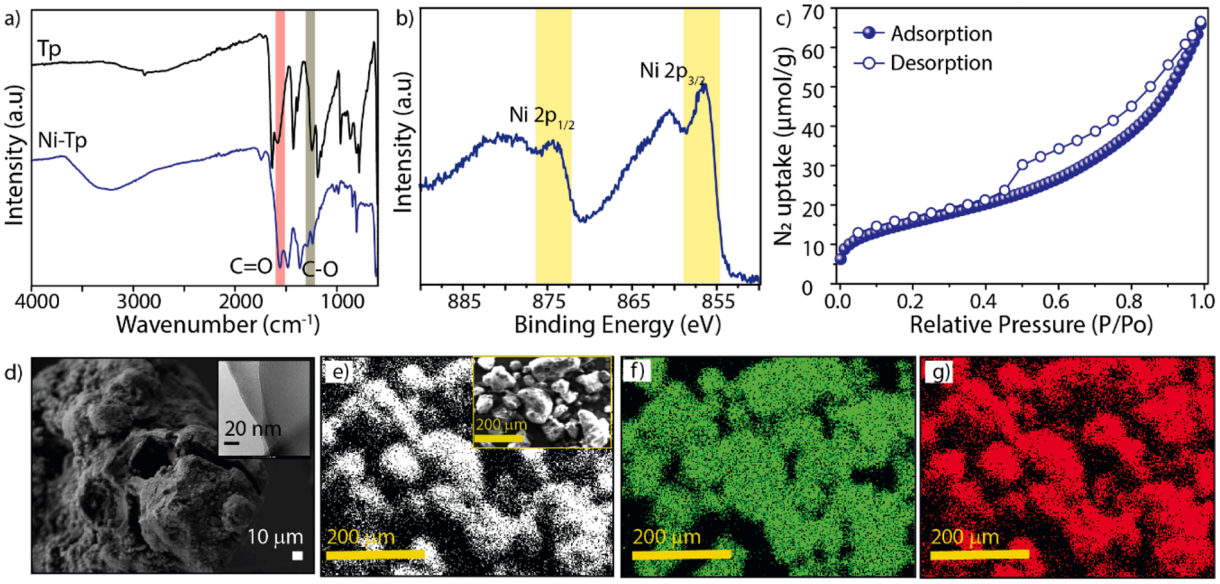

Fig. 2. (a) FT-IR profiles of Ni-Tp with Tp linker. (b) the XPS profile of Ni-Tp shows the chemical state of Ni in the MOF. (c) N_2 gas adsorption isotherm of Ni-Tp with a BET surface area of 109 $m^2\ g^{-1}$. (d) SEM images of Ni-Tp. Inset: TEM image of Ni-Tp. (e) EDX images show carbon (grey) (INSET: The original SEM images for the elemental mapping), (f) nickel (green), and (g) oxygen (red) distribution in Ni-Tp. (For interpretation of the references to color in this figure legend, the reader is referred to the web version of this article.)

Ni $2p_{1/2}$ (874.36 eV) with corresponding weak satellite peaks. The higher binding energy of Ni indicates its + 2 oxidation state [15]. The Ni-Tp is synthesized in the presence of water, which may allow water molecules to coordinate with the nickel in the framework. A weak and broad peak observed at ~3000–3500 cm^{-1} in the FT-IR spectrum of Ni-Tp indicates the presence of water in the framework (Fig. S5). Additionally, the Fourier-transformed extended X-ray absorption fine structure (EXAFS) data suggest the potential coordination of water molecules with nickel. For more details, please refer to the in-situ and ex-situ analysis section and Table S3.

To analyze the broad-range synthetic feasibilities of Ni-Tp, we have conducted the synthesis in different reaction conditions such as temperature, time, and varying the nickel salt precursor. The formation of semicrystalline Ni-Tp at even low temperatures (60 °C for 5 h) treatment indicates the energy-friendly nature of the synthesis (Fig. S7). Notably, Ni-Tp was formed within 1 h at 90 °C (Fig. S8 –S9). Moreover, the PXRD and FT-IR characteristic profiles of Ni-Tp were maintained even after 72 h of treatment in water and various organic solvents such as DMA, THF, acetonitrile, and toluene (Figs. S10–S11). It signifies the structural and chemical stability of Ni-Tp with the strong coordinative interaction of metal ions with Tp to resist any solvation effect. Moreover, the retained PXRD and FT-IR profiles showed the chemical stability of Ni-Tp towards 1 M KOH treatment (Figs. S12-S13). When we varied the nickel salts counter ions (chloride, nitrate, acetate, and acetylacetonate), only acetate and acetylacetonate led to successful identical crystallinity. On the other hand, nickel chloride does not interact with Tp as reflected by PXRD, which corresponds to Tp alone. Nickel nitrate was also amorphous under the same synthesis conditions (Figs. S14-16). Hereinafter, $Ni(OAc)_2{\cdot}4H_2O$ was used in further exploration due to the optimum crystallinity and stability of the resulting product.

The critical role of the C_3 symmetric salicylaldehyde functional group for the strong coordination with Ni^{2+} was understood from a control-study of functional groups (Figs. S17–S21). The reaction of Ni^{2+} with sole OH group functionalized C_3 symmetric phloroglucinol (Pg) yielded a light-brown powder (Ni-Pg). Meanwhile, the reaction with 2-hydroxytriformylbenzene (Ht) with Ni^{2+} resulted in a light-green color powder (Ni-Ht). The PXRD profiles indicate a crystalline pattern before washing Ni-Pg and Ni-Ht. Again, FT-IR profiles showed new peaks for Ni-Pg and Ni-Ht, indicating the coordination possibilities between metal and organic linkers. However, these materials exhibited relatively lower stability in highly polar solvents such as DMA. The poor solvent stability could be attributed to the lack of strong interactions between the metal ions and the organic linkers, which results in the limited growth of the framework. In this case, 'Pg' contains only –OH groups as functional moieties for interaction with metal ions, whereas 'Ht' features one salicylaldehyde functional pocket and two additional C═O groups. In both instances, the framework growth is restricted due to the absence of multiple salicylaldehyde functional pockets and their symmetric distribution. This underscores the critical role of C_3-symmetric salicylaldehyde-type interactions between metal ions and organic monomers in facilitating the growth of the framework in 2D space.

Thermogravimetric analysis (TGA) showed the thermal stability of Ni-Tp in an inert (N_2) atmosphere (Fig. S22). The TGA plot of Ni-Tp indicates thermal stabilities up to 300 °C with 91.7 % of weight retention. The porosity features of Ni-Tp were analyzed using N_2 gas adsorption isotherm at 77 K (Fig. 2c). The Ni-Tp exhibited a type-II adsorption isotherm with a Brunauer-Emmett-Teller (BET) surface area of 109 $m^2\ g^{-1}$. Non-local density functional theory (NLDFT) pore size distribution of Ni-Tp showed a pore size around 1.1 nm (Fig. S23). Transmission electron microscopy (TEM) imaging revealed 2D sheet-like morphology for Ni-Tp on a nanoscopic scale (Fig. 2d (inset) and Fig. S24). Scanning electron microscopy (SEM) displayed macroporous surface features of Ni-Tp (Fig. 2d). The elemental mapping of these MOFs shows a uniform distribution of carbon (grey), nickel (green), and oxygen (red) elements (Fig. 2e–f; Fig. S25).

The chemical bonding between Tp and Ni^{2+} offers the π-d conjugation throughout the 2D layer of Ni-Tp. The extended π-d conjugation facilitates a lower band gap for the material with semiconductive properties. The solid-state ultra-violet (UV)-visible spectroscopic investigation showed a broad range of visible-light absorption from 700 nm to 450 nm with wavelength maxima of 640 nm and 507 nm (Fig. S26a). Moreover, the Tauc plot suggested an optical-electronic band gap of 1.5 eV (Fig. S26b). To understand the intrinsic electrical conductivity of Ni-Tp, a 4-probe measurement was performed, which suggests a moderate sheet conductivity of ~40 µS m^{-1} (25 kΩ m^{-1}) at room temperature (Fig. S27 and Table S2). For an electrode with a common precatalyst film thickness of 1 µm, this sheet conductivity yields a resistivity of 0.25 Ω. Thus, following Ohm law, at a current density of 100 mA cm^{-2}, a

potential drop of 25 mV would result. We note that the resistivity during catalysis might be much lower as the applied potential and the proton active electrolyte can cause proton-coupled electron transfers, leading to transportable electron holes that facilitate charge transport [16].

3.2. Electrocatalytic properties of Ni-Tp and HMF oxidation

We applied a binder-free electrophoretic deposition approach to fabricate an electrode coated with Ni-Tp (see Supporting Information for details). This method was used to manufacture thin films on nickel foam (NF) (Ni-Tp loading 0.6 mg cm^{-2}, Ni loading 0.2 mg cm^{-2}, called Ni–Tp–NF) and fluorine-doped tin oxide (Ni-Tp loading 0.3 mg cm^{-2}, Ni loading 0.1 mg cm^{-2}, called Ni-Tp-FTO, see Fig. S28 for a FT-IR measurement of the Ni-Tp powder and film). Ni–Tp–NF was used for the electrocatalytic tests due to NF's better conductivity and higher surface area. High surface areas are crucial for HMF oxidation as it has been shown that the reaction can be limited by substrate mass transport [17–19]. However, NF is unsuitable for many characterization methods, as it also contains Ni and has no flat surface. Thus, the precatalyst was also deposited on FTO. First of all, linear scanning voltammetry (LSV) of Ni–Tp–NF was performed in two electrolytes, 1 M KOH and 1 M KOH with 30 mM HMF, to investigate the suitability of Ni-Tp-NF and Ni-Tp-FTO for the selective oxidation of HMF (Fig. 3a and S29). For both electrodes, a substantially higher current density is observed in the HMF-containing electrolyte [20]. This additional current can be assigned to the oxidation of HMF. For both electrodes, the onset of this additional current is at around 1.37 V versus the reversible hydrogen electrode (V_{RHE}), concurrent with the nickel(II) oxidation peak in HMF-free alkaline electrolyte (green line in Fig. 3a and S29). This peak's potential is the same for Ni-Tp-NF and Ni-Tp-FTO, and the nickel oxidation peak for bare NF is severely smaller. Thus, we assign it to the oxidation of Ni-Tp's nickel(II) centers (or a phase formed in-situ out of the Ni-Tp) and not to nickel atoms of the NF. In the HMF-free electrolytes, a steep rise in the current density can also be observed (green line Fig. 3a). This rise onsets 110 mV after the nickel(II) redox peak at around 1.48 V_{RHE}, concurrent with strong bubble formation, and we assign it to the oxygen evolution reaction (OER). Furthermore, the bare NF reference and an NF with nickel (oxy)hydroxide showed much lower current densities for HMF oxidation and the OER (Fig. 3a, black and grey lines and for a comparison with nickel (oxy)hydroxide see Fig. S30). Bare FTO shows almost no activity (Fig. S29).

The observed potentiodynamic behavior is typical for Ni centers in alkaline environments.[9a, 11] For such systems, the oxidation of nickel (II) leads to the formation of nickel(III) and $Ni^{III+\delta}$–$O^{-II+(1-\delta)}$ (active oxygen) [17,21–23]. Both of these Ni species have been shown to be able to oxidize HMF [18, 3 25]. Nevertheless, for the OER, monometallic nickel species require a higher potential as the potential determining step has been found to be the O—O bond formation [21]. The range for the selective oxidation of alcohols and aldehydes groups, such as those present in HMF, is between the potential required for the nickel(II) oxidation and the potential required for the O—O bond formation (Fig. 3a red arrow). No HMF oxidation occurs at lower potentials, and at higher potentials, the OER occurs as a side reaction (see Fig. S31 for an estimation of the potential-dependent Faradaic efficiency) [17,24].

In view of the analysis above, we have chosen 1.47 V_{RHE} for the bulk oxidation of HMF. During this bulk oxidation, the reaction mixture was stirred to minimize substrate mass transport limitations [17,25]. Initially, the current density is above 200 mA cm^{-2} and then consistently drops (Fig. 3b) as the reaction rate decreases with decreasing HMF substrate concentration. After 52 min, the minimum charge (for 100 % Faradaic efficiency) required to completely oxidize HMF to FDCA is reached. At this time, a proton nuclear magnetic resonance spectrum (NMR) of the reaction has been recorded with an internal standard (maleic acid, Fig. S32). This quantification showed that 96 ± 4 % of the HMF has been converted into the desired product, FDCA. Thus, considering the transferred charge, the selectivity and faradaic efficiency are quantitative (see Supporting Information for details on the calculation, see Fig. S33 for a 24 h stability measurement). As a reference, the same experiment has been performed with bare NF. The bare NF shows a substantially lower current density, and after the same time at the same potential, only 8 % of the HMF has been converted to FDCA.

3.3. Reconstruction of the MOF revealed by ex- and in-situ analyses

Electrocatalysts behave dynamically during reaction conditions [26–29]. In this regard, the high applied potentials and the harsh alkaline conditions (pH 13.89) potentially alter the structure of the original Ni-Tp phase [20]. To investigate the structural evolution, the HMF oxidation (HMFO) is performed with Ni-Tp-FTO for 60 min at 25 mA cm^{-2} with an excess amount of HMF (100 mM, Fig. S34). Afterward, the sample was rinsed with deionized water and air-dried, which is referred to as Ni-Tp-HMFO. The FT-IR of Ni-Tp-HMFO shows that all

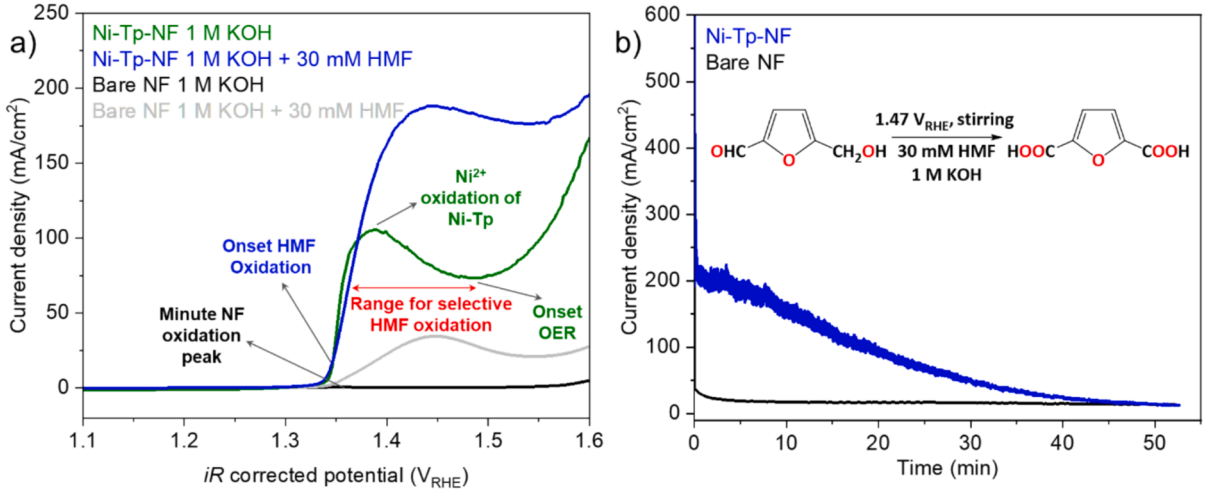

Fig. 3. (a) linear scan voltammetry data (10 mV/s, *iR* corrected, no stirring) of Ni-Tp deposited in a binder-free way on nickel foam (Ni-Tp-NF, Ni-Tp loading 0.6 mg cm^{-2}, Ni loading 0.2 mg cm^{-2}) in 1 M KOH (pH = 13.89) and 1 M KOH with 30 mM 5-hydroxymethylfuran (HMF) [16–18]. Relevant onsets, peaks, and potential ranges are depicted. Bare nickel foam (NF) is added as a reference. Data of the same measurement for a fluorine-doped tin oxide (FTO) substrate is shown in Fig. S29. (b) Chronoamperometric bulk oxidation of HMF to FDCA (*iR* corrected, stirring, 10 ml total electrolyte volume) with Ni-Tp-NF and bare NF. ^{1}H nuclear magnetic resonance spectra for the reaction mixtures are provided in Fig. S32.

peaks of the original Ni-Tp phase are still present (Fig. S35). However, the OH peak at ~ 3300 cm^{-1} is much larger, indicating the partial reconstruction of the Ni-Tp to a new, hydroxide-containing phase. We scratched off the material from Ni–Tp–HMFO and investigated it using electron microscopy. SEM reveals no apparent change in the morphology (Fig. S36), and an elemental mapping shows a homogenous distribution of nickel, carbon, and oxygen similar to the as-prepared material. Additionally, a smaller quantity of potassium is homogeneously distributed in the material. TEM images of Ni–Tp–HMFO reveal the presence of two phases in the material (Fig. 4) after catalysis. One is the original Ni-Tp phase (Fig. 4a–d), also detected by FT-IR (Fig. S35). It shows the same morphology and selected area electron diffraction (SAED) pattern as the as-prepared Ni-Tp (Fig. 4a–d). A second phase with a different morphology is present (Fig. 4e–h).

This phase comprises nanoparticles with sizes between 10 and 50 nm. Notably, the SAED pattern (Fig. 4g) shows the typical diffraction spots for layered (oxy)hydroxides [30] and the lattice spacings could be assigned to nickel (oxy)hydroxides [JCPDS 6-75]. These observations are confirmed by the high-resolution TEM images (Fig. 4h) and their fast Fourier transform (inset of Fig. 4h). Nickel (oxy)hydroxides have previously been reported to form under alkaline oxidizing conditions and are also the thermodynamically stable Ni phase (see Pourbaix diagram Fig. 5a) [27,30,31]. We note that SEM energy-dispersive X-ray spectroscopy (EDX) has shown that potassium entered the Ni–Tp–HMFO phase. As previously reported, this potassium is most likely intercalated into the nickel oxyhydroxide [32]. Thus, the formula of the newly formed phase is likely $K_xNiO_yH_z$. The XPS profile of Ni-Tp after catalysis indicates a lower binding energy shift of the O1s peak (531.19 eV) compared to before catalysis (532.69 eV, Fig. S37). Furthermore, the presence of potassium was noted at the binding energies of 292.67 eV and 295.80 eV for the $K2p_{3/2}$ and $K2p_{1/2}$ peaks, respectively.

The Raman spectrum of Ni–Tp–HMFO shows all the peaks of the as-prepared Ni-Tp and an additional peak in the region for nickel oxides (Fig. S38). To gain more information into the dynamic behavior of the material during electrocatalysis, quasi-in-situ Raman spectroscopy was performed by freeze-quenching the samples in liquid nitrogen. A potential before (Fig. 3a for LSV, 1.25 V_{RHE}) and after (1.47 V_{RHE}, where the bulk electrolysis was performed) the nickel(II) oxidation feature was chosen in 1 M KOH with 30 mM HMF. This oxidation feature is consistent with the Pourbaix diagram (Fig. 5a), which indicates a phase transition around this potential from nickel(II) hydroxide to nickel(III) oxyhydroxide [31]. In this regard, at 1.25 V_{RHE}, the Raman spectrum shows a single peak consistent with nickel(II) hydroxide[17]. At 1.47 V_{RHE}, two peaks appear typical for nickel(III-IV) oxyhydroxide [17]. These findings align with the formation of the $K_xNiO_yH_z$ phase identified by TEM. Furthermore, the materials change their color (Fig. 5a insets). At 1.25 V_{RHE}, the electrode has the beige color of the as-prepared Ni-Tp powder, consistent with the previously reported transparency of hydrated nickel(II) hydroxide phases [33]. At 1.47 V_{RHE}, the electrode turns black, consistent with nickel(III) oxyhydroxide [33]. The observation that all Ni is in the oxidized form during the reaction also indicates that the oxidation of Ni is not the rate-determining step, as it accumulates (nickel(III) has been shown to oxidize alcohols and aldehydes chemically) [22,34]. Thus, the rate-determining step should be the oxidation of HMF by the nickel(III). Another possibility is that the Ni charges accumulate due to insufficient substrate availability [19].

The ex-situ and quasi-in-situ characterizations confirm a partial reconstruction of Ni–Tp to nickel (oxy)hydroxide nanoparticles. This new phase behaves as predicted by the nickel Pourbaix diagram (Fig. 5a). The red arrow in Fig. 5a shows the position of the two investigated potentials with the respective thermodynamically stable nickel hydroxide and nickel oxyhydroxide phases. When switching the potential from 1.25 to 1.47 V_{RHE}, all Ni centers are oxidized, as no peaks for the nickel(II) hydroxide phase remain in the Raman spectrum, and the sample turns black. Furthermore, the absence of any Raman features for nickel(III) oxyhydroxide and the transparency at 1.25 V_{RHE} show that all Ni of the in-situ formed $K_xNiO_yH_z$ phase can be reduced again. Thus, all Ni sites are redox active. To be redox active, they must have access to the electrolyte, as a proton exchange is involved for charge balance ($Ni(OH)_2 \rightarrow NiOOH + e^- + H^+$). Furthermore, the sites must be anodically wired to enable electron transport. These two properties are also prerequisites for participating in the HMF oxidation. All Ni sites of the newly formed nickel (oxy)hydroxide phase fulfill these prerequisites, indicating that almost all sites can potentially be catalytically active. This high active site availability is likely accomplished through the reconstruction of the MOF precatalyst, wherein the nickel centers are highly dispersed. This dispersion enables the formation of a nickel (oxy) hydroxide phase comprising nanoparticles, exposing many catalytically active Ni centers, which is one of the two main advantages of the herein-used approach. We note that all data indicate that the active sites are

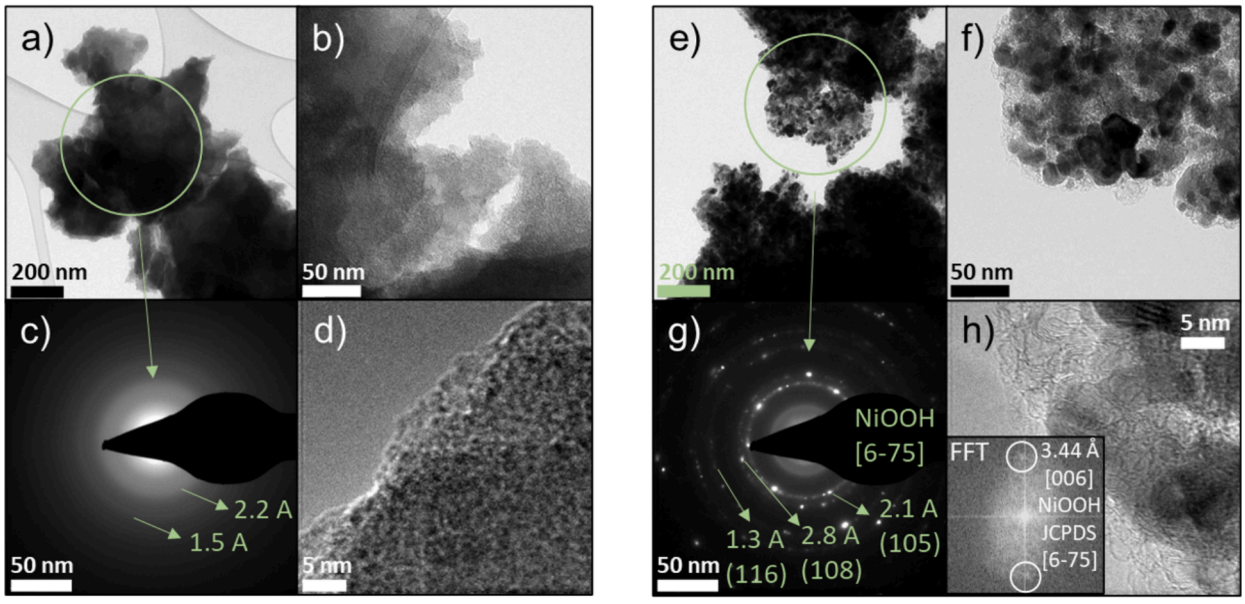

Fig. 4. Transmission electron microscopy (TEM) of the Ni–Tp after HMF oxidation (Ni-Tp-FTO). The samples were scratched off for this investigation. (a–d) show the as-prepared Ni-Tp phase, which still remains in the sample. (e–h) show the newly formed nickel oxyhydroxide nanoparticles, which formed during the reaction.

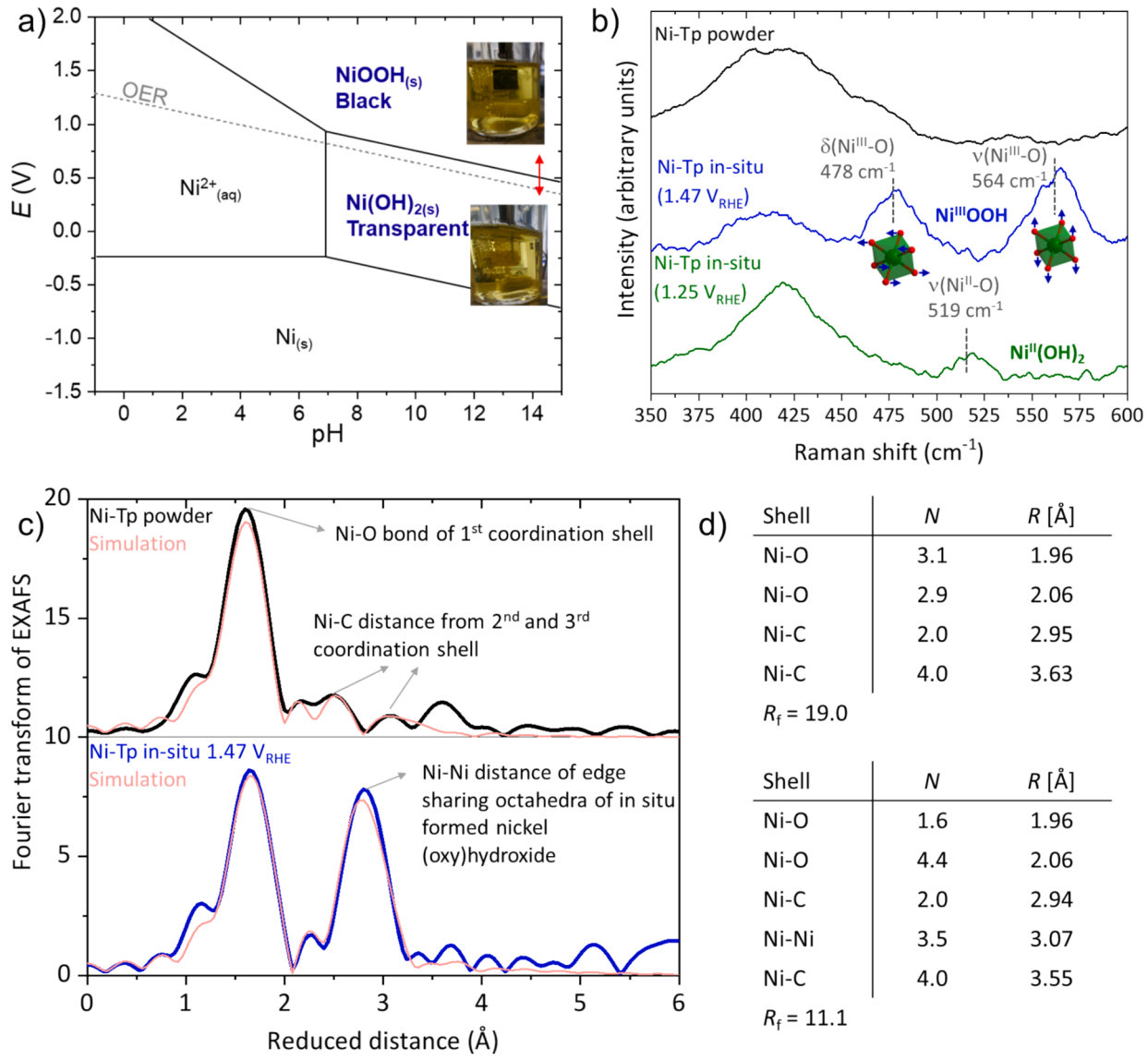

d)

Shell	*N*	*R* [Å]
Ni-O	3.1	1.96
Ni-O	2.9	2.06
Ni-C	2.0	2.95
Ni-C	4.0	3.63

R_f = 19.0

Shell	*N*	*R* [Å]
Ni-O	1.6	1.96
Ni-O	4.4	2.06
Ni-C	2.0	2.94
Ni-Ni	3.5	3.07
Ni-C	4.0	3.55

R_f = 11.1

Fig. 5. (a) Pourbaix diagram of nickel with two images of the electrode in aqueous 1 M KOH with 30 mM HMF at 1.47 V_{RHE} (top image with black electrode, NiOOH) and 1.25 V_{RHE} (bottom image, beige electrode from the Ni-Tp, $Ni(OH)_2$ transparent). (b) In-situ Raman spectroscopy in the same conditions as the images of (a), showing the typical vibrations of octahedrally coordinated [NiO_6] in nickel(II) hydroxide (green) and nickel(III/IV) oxyhydroxide (blue). (c) In-situ, Fourier-transformed extended X-ray absorption fine structure (EXAFS) data of the as-prepared Ni-Tp powder and Ni-Tp-FTO that has been conditioned at 25 mA/cm^2 in aqueous 1 M KOH with 100 mM HMF and subsequently freeze quenched after 5 min at a potential of 1.47 V_{RHE}. This freeze-quenched sample is called Ni-Tp in-situ. The k^3-weighted data is shown in Fig. S39 (Supporting Information). Simulations of the data are shown as thin red lines. The respective simulation parameters and detailed explanations of the simulations are shown partly in (d) and extensively in Table S3. The Ni-Tp powder phase could be simulated with a model based on the crystal structure shown in Fig. 1. However, the simulation succeeded only with six oxygen neighbors around the nickel. Therefore, we suggest that two additional water molecules are coordinated to the nickel centers. The simulation of the Ni-Tp in-situ sample was only successful when the coexistence of a Ni-Tp and nickel (oxy) hydroxide phase was assumed. The nickel-oxygen and nickel-nickel bond distances, as well as the XANES (Fig. S40) data indicate that the newly formed phase is mainly nickel(II) hydroxide. (For interpretation of the references to color in this figure legend, the reader is referred to the web version of this article.)

located in the nickel (oxy)hydroxide phase. However, this does not prove that the nickel sites of the Ni-Tp do not contribute to the catalysis at all.

We have performed in-situ X-ray absorption spectroscopy to provide additional structural proof for the coexistence of the Ni-Tp and nickel (oxy)hydroxide phase. In this regard, we collected data for the as-prepared Ni-Tp powder and a sample freeze-quenched in situ at 1.47 V_{RHE}, analogously to the in-situ Raman investigations. The obtained data is shown in Fig. 5c and 5d (Fourier-transformed extended X-ray absorption fine structure (EXAFS) data), in Fig. S39 (k^3-weighted EXAFS data), Fig. S40 (X-ray absorption near edge structure (XANES) data), and Table S3 (detailed description of the EXAFS simulation parameters and models). For the as-prepared Ni-Tp powder sample, the simulation of the EXAFS data was only successful with six coordinating oxygens (see caption of Table S3 for details). Therefore, we propose that the nickel in Ni-Tp is coordinated by four oxygens of the Tp-linker in a quadratic planar fashion and, additionally, by two water molecules. For the in-situ sample, the analysis of this data unambiguously shows the presence of a nickel (oxy)hydroxide phase, as a large peak typical for the nickel-nickel distance of nickel (oxy)hydroxide appears in the EXAFS data (Fig. 5c, blue line just below 3 Å). Furthermore, the in-situ EXAFS data simulations were only successful when a remaining Ni-Tp was included in the model (Table S3 for details). This observation confirms our hypothesis that a hybrid Ni-Tp nickel (oxy)hydroxide structure forms in-situ and drives the high electrocatalytic performance.

4. Conclusion

Overall, the work highlights the application of salicylaldehydate-linked and π-d conjugated Ni-Tp for electrocatalytic conversion of HMF to FDCA, achieving a remarkable selectivity and Faradaic efficiency (both 96 ± 4 %). Ni-Tp, is synthesized via a solid-state protocol and plays a pivotal role in the electrocatalytic process by serving as both a source of active electrocatalytic sites, particularly nickel (oxy)hydroxide nanoparticles, and an essential electron transport platform. Notably, ex- and in-situ characterizations revealed that all these electrocatalytic sites are redox active and benefit from effective contact with the electrolyte. Thus, the Ni-Tp is an ideal precatalyst in terms of nickel (oxy)hydroxide active site exposure. The synergy of the uniform dispersion of Ni atoms and π-d conjugation for electron transport in Ni-Tp contributes to substantial mass and charge transport and ultimately enhances the catalytic activity. With its cost-effective and scalable solid-state production and its efficient performance as a precatalyst, Ni-Tp demonstrates significant potential for practical applications in biomass conversion into commercially valuable chemicals. We are hopeful that the next phase of this work will focus on scaling up the production of Ni-Tp and exploring its practical utility in large-scale biomass conversion.

CRediT authorship contribution statement

Abdul Khayum Mohammed: Writing – original draft, Visualization, Validation, Methodology, Investigation, Formal analysis, Data curation, Conceptualization. **J.Niklas Hausmann:** Writing – original draft, Visualization, Validation, Methodology, Investigation, Formal analysis, Data curation, Conceptualization. **Safa Gaber:** Writing – original draft, Validation, Methodology, Investigation, Formal analysis, Data curation. **Pilar Pena Sánchez:** Writing – review & editing, Methodology, Formal analysis, Data curation. **Felipe Gándara:** Writing – review & editing, Validation, Supervision, Software, Formal analysis. **Konstantin Laun:** Writing – review & editing, Formal analysis, Data curation. **Ingo Zebger:** Writing – review & editing, Formal analysis, Data curation. **Prashanth W. Menezes:** Writing – review & editing, Validation, Supervision, Resources, Funding acquisition, Formal analysis, Conceptualization. **Dinesh Shetty:** Writing – review & editing, Validation, Supervision, Resources, Project administration, Funding acquisition, Formal analysis, Conceptualization.

Declaration of competing interest

The authors declare the following financial interests/personal relationships which may be considered as potential competing interests: Dinesh Shetty has patent pending to US Patent App. 18/243,310. If there are other authors, they declare that they have no known competing financial interests or personal relationships that could have appeared to influence the work reported in this paper.

The Supporting Information is available: Details on general materials and instruments, experimental details for the preparations, characterizations, and Figs. S1–S33 and Tables S1 and S2, including theoretical models, PXRD, FT-IR, XPS, TGA, Gas adsorption, TEM, solid-state UV–visible spectrum, electrical conductivity, ^{1}H NMR, Raman spectra and electrochemical measurements.

Acknowledgements

AKM, JNH, and SG contributed equally to this work. AKM, SG, and DS acknowledge Khalifa University, Abu Dhabi for the generous support of this research. DS acknowledges the financial support from the Khalifa University Competitive Internal Research Award (CIRA-2021). DS acknowledges resource support under the Center for Catalysis and Separations (CeCaS, grantRCII-2018-024). We acknowledge Johannes Schmidt for the XPS measurement and Gonela Vijaykumar for initial electrochemical experiments. JNH. and PWM acknowledge support from the German Federal Ministry of Education and Research in the framework of the projects “Catlab” (03EW0015A/B) and “PrometH2eus” (03HY105C).

Appendix A. Supplementary data

Supplementary data to this article can be found online at https://doi.org/10.1016/j.jcis.2025.137630.

Data availability

Data is included within the supplementary information

References

[1] H.C. Zhou, J.R. Long, O.M. Yaghi, Introduction to metal–organic frameworks, Chem. Rev. 112 (2012) 673–674.
[2] M. Hmadeh, Z. Lu, Z. Liu, F. Ga'ndara, H. Furukawa, S. Wan, V. Augustyn, R. Chang, L. Liao, F. Zhou, E. Perre, V. Ozolins, K. Suenaga, X. Duan, B. Dunn, Y. Yamamto, O. Terasaki, O.M. Yaghi, New porous crystals of extended metal-catecholates, Chem. Mater. 24 (2012) 3511–3513.
[3] D. Sheberla, L. Sun, M.A. Blood-Forsythe, S. Er, C.R. Wade, C.K. Brozek, A. Aspuru-Guzik, M. Dinca, High electrical conductivity in Ni_3(2,3,6,7,10,11-hexaiminotriphenylene)$_2$, a semiconducting metal–organic graphene analogue, J. Am. Chem. Soc. 136 (2014) 8859–8862.
[4] T. Kambe, R. Sakamoto, K. Hoshiko, K. Takada, M. Miyachi, J.H. Ryu, S. Sasaki, J. Kim, K. Nakazato, M. Takata, H. Nishihara, π-Conjugated nickel bis(dithiolene) complex nanosheet, J. Am. Chem. Soc. 135 (2013) 2462–2465.
[5] K.W. Nam, S.S. Park, R. dos Reis, V.P. Dravid, H. Kim, C.A. Mirkin, J.F. Stoddart, Conductive 2D metal-organic framework for high-performance cathodes in aqueous rechargeable zinc batteries, Nat. Commun. 10 (2019) 4948.
[6] H. Zhong, M. Wang, G. Chen, R. Dong, X. Feng, Two-Dimensional Conjugated metal–organic frameworks for electrocatalysis: opportunities and challenges, ACS Nano 16 (2022) 1759–1780.
[7] M. Cai, Y. Zhang, Y. Zhao, Q. Liu, Y. Li, G. Li, Two-dimensional metal–organic framework nanosheets for highly efficient electrocatalytic biomass 5-(hydroxymethyl)furfural (HMF) valorization, J. Mater. Chem. A 8 (2020) 20386–20392.
[8] Y. Zhang, N. Kornienko, Conductive metal-organic frameworks bearing $M-O_4$ active sites as highly active biomass valorization electrocatalysts, ChemSusChem 15 (2022) e202101587.
[9] T. Kahlstorf, J.N. Hausmann, T. Sontheimer, P.W. Menezes, Challenges for hybrid water electrolysis to replace the oxygen evolution reaction on an industrial scale, Global Chall. 7 (2023) 2200242.
[10] C. Guo, Y. Huo, Q. Zhang, K. Wan, G. Yang, Z. Liu, F. Peng, MOF material-derived bimetallic sulfide CoxNiyS for electrocatalytic oxidation of 5-hydroxymethylfurfural, Nanomaterials 13 (2023) 2318.
[11] Y. Feng, K. Yang, R.L. Smith Jr., X. Qi, Metal sulfide enhanced metal–organic framework nanoarrays for electrocatalytic oxidation of 5-hydroxymethylfurfural to 2, 5-furandicarboxylic acid, J. Mater. Chem. A 11 (2023) 6375–6383.
[12] Y. Feng, W. Jia, G. Yan, X. Zeng, J. Sperry, B. Xu, Y. Sun, X. Tang, T. Lei, L. Lin, Insights into the active sites and catalytic mechanism of oxidative esterification of 5-hydroxymethylfurfural by metal-organic frameworks-derived N-doped carbon, J. Catal. 381 (2020) 570–578.
[13] X.-J. Bai, W.-X. He, X.-Y. Lu, Y. Fu, W. Qi, Electrochemical oxidation of 5-hydroxymethylfurfural on ternary metal–organic framework nanoarrays: enhancement from electronic structure modulation, J. Mater. Chem. A 9 (2021) 14270–14275.
[14] A.K. Mohammed, P.P. Sa'nchez, A. Pandikassala, S. Gaber, A.A. AlKhoori, T. Skorjanc, K. Polychronopoulou, S. Kurungot, F. Ga'ndara, D. Shetty, Salicylaldehyde coordinated two-dimensional-conjugated metal–organic frameworks, Chem. Commun. 59 (2023) 2608–2611.
[15] Z. Meng, A. Aykanat, K.A. Mirica, Two-dimensional chemiresistive covalent organic framework with high intrinsic conductivity, J. Am. Chem. Soc. 141 (2019) 2046–2053.
[16] C.N. Brodsky, D.K. Bediako, C. Shi, T.P. Keane, C. Costentin, S.J.L. Billinge, D. G. Nocera, Proton-electron conductivity in thin films of a cobalt-oxygen evolving catalyst, ACS Appl. Energy Mater. 2 (2019) 3–12.
[17] J.N. Hausmann, P.V. Menezes, G. Vijaykumar, K. Laun, T. Diemant, I. Zebger, T. Jacob, M. Driess, P.W. Menezes, In-liquid plasma modified nickel foam: NiOOH/NiFeOOH active site multiplication for electrocatalytic alcohol, aldehyde, and water oxidation, Adv. Energy Mater. 12 (2022) 2202098.
[18] X. Pang, H. Bai, H. Zhao, W. Fan, W. Shi, Efficient electrocatalytic oxidation of 5-hydroxymethylfurfural coupled with 4-nitrophenol hydrogenation in a water system, ACS Catal. 12 (2022) 1545–1557.
[19] T. Kahlstorf, J.N. Hausmann, I. Mondal, K. Laun, I. Zebger, T. Sontheimer, P. W. Menezes, Water-soluble nickel and iron salts for hydroxymethylfurfural (HMF) and water oxidation: The simplest precatalysts? Green Chem. 25 (2023) 8679–8686.
[20] J.N. Hausmann, B. Traynor, R.J. Myers, M. Driess, P.W. Menezes, The pH of aqueous NaOH/KOH solutions: A critical and non-trivial parameter for electrocatalysis, ACS Energy Lett. 6 (2021) 3567–3571.

[21] H.B. Tao, Y. Xu, X. Huang, J. Chen, L. Pei, J. Zhang, J.G. Chen, B.A. Liu, A general method to probe oxygen evolution intermediates at operating conditions, Joule 3 (2019) 1498–1509.
[22] M.T. Bender, Y.C. Lam, S.H. Schiffer, K.-S. Choi, Unraveling two pathways for electrochemical alcohol and aldehyde oxidation on NiOOH, J. Am. Chem. Soc. 142 (2020) 21538–21547.
[23] D.A. Kuznetsov, B. Han, Y. Yu, R.R. Rao, J. Hwang, Y.R. Leshkov, Y.S. Horn, Tuning redox transitions via inductive effect in metal oxides and complexes, and implications in oxygen electrocatalysis, Joule 2 (2018) 225–244.
[24] Y. Gao, L. Ge, H. Xu, K. Davey, Y. Zheng, S.-Z. Qiao, Electrocatalytic refinery of biomass-based 5-hydroxymethylfurfural to fine chemicals, ACS Catal. 13 (2023) 11204–11231.
[25] S. Barwe, J. Weidner, S. Cychy, D.M. Morales, S. Dieckhöfer, D. Hiltrop, J. Masa, M. Muhler, W. Schuhmann, Electrocatalytic oxidation of 5-(hydroxymethyl) furfural using high-surface-area nickel boride, Angew. Chem. Int. Ed. 57 (2018) 11460.
[26] X. Liu, J. Meng, J. Zhu, M. Huang, B. Wen, R. Guo, L. Mai, Comprehensive understandings into complete reconstruction of precatalysts: Synthesis, applications, and characterizations, Adv. Mater. 33 (2021) 2007344.
[27] B.R. Wygant, K. Kawashima, C.B. Mullins, Catalyst or precatalyst? The Effect of Oxidation on Transition Metal Carbide, Pnictide, and Chalcogenide Oxygen Evolution Catalysts, ACS Energy Lett. 3 (2018) 2956–2966.
[28] J.N. Hausmann, P.W. Menezes, Why should transition metal chalcogenides be investigated as water splitting precatalysts even though they transform into (oxyhydr)oxides? Curr. Opin. Electrochem. 34 (2022) 100991.
[29] J.N. Hausmann, S. Mebs, K. Laun, I. Zebger, H. Dau, P.W. Menezes, M. Driess, Understanding the formation of bulk- and surface-active layered (oxy)hydroxides for water oxidation starting from a cobalt selenite precursor, Energ. Environ. Sci. 13 (2020) 3607–3619.
[30] B. Dasgupta, J.N. Hausmann, R.B. Suito, S. Kalra, K. Laun, I. Zebger, M. Driess, P. W. Menezes, A facile molecular approach to amorphous nickel pnictides and their reconstruction to crystalline potassium-intercalated γ-NiOOHx enabling high-performance electrocatalytic water oxidation and selective oxidation of 5-hydroxymethylfurfural, Small 19 (2023) 2301258.
[31] G.K. Schweitzer, L.L. Pesterfield, The aqueous chemistry of the elements, Oxford University Press, 2010.
[32] F. Dionigi, Z. Zeng, I. Sinev, T. Merzdorf, S. Deshpande, M.B. Lopez, S. Kunze, I. Zegkinoglou, H. Sarodnik, D. Fan, A. Bergmann, J. Drnec, J.F. Araujo, M. Gliech, D. Teschner, J. Zhu, W.X. Li, J. Greeley, B.R. Cuenya, P. Strasser, In-situ structure and catalytic mechanism of NiFe and CoFe layered double hydroxides during oxygen evolution, Nat. Commun. 11 (2020) 2522.
[33] A. Mavrič, M. Fanetti, Y. Lin, M. Valant, C. Cui, Spectroelectrochemical tracking of nickel hydroxide reveals its irreversible redox states upon operation at high current density, ACS Catal. 10 (2020) 9451–9457.
[34] M. Fleischmann, K. Korinek, D. Pletcher, The kinetics and mechanism of the oxidation of amines and alcohols at oxide-covered nickel, silver, copper, and cobalt electrodes, J. Chem. Soc. Perkin Trans. 2 (1972) 1396–1403.